Vortex properties in the extended supersolid phase of dipolar Bose-Einstein condensates

Francesco Ancilotto [1,2] Manuel Barranco,[3,4] Martí Pi,[3,4] and Luciano Reatto [5]

[1]*Dipartimento di Fisica e Astronomia "Galileo Galilei" and CNISM, Università di Padova, via Marzolo 8, 35122 Padova, Italy*
[2]*CNR-IOM, via Bonomea, 265 - 34136 Trieste, Italy*
[3]*Departament FQA, Facultat de Física, Universitat de Barcelona, Avenida Diagonal 645, 08028 Barcelona, Spain*
[4]*Institute of Nanoscience and Nanotechnology (IN2UB), Universitat de Barcelona, 08028 Barcelona, Spain*
[5]*Dipartimento di Fisica, Università degli Studi di Milano, via Celoria 16, 20133 Milano, Italy*

We study the properties of singly quantized linear vortices in the supersolid phase of a dipolar Bose-Einstein condensate at zero-temperature modeling ^{164}Dy atoms. The system is extended in the *x*-*y* plane and confined by a harmonic trap in the polarization direction *z*. Our study is based on a generalized Gross-Pitaevskii equation. We characterize the ground state of the system in terms of spatial order and superfluid fraction and compare the properties of a single vortex and of a vortex dipole in the superfluid phase (SFP) and in the supersolid phase (SSP). At variance with a vortex in the SFP, which is free to move in the superfluid, a vortex in the SSP is localized at the interstitial sites and does not move freely. We have computed the energy barrier for motion from an equilibrium site to another. The fact that the vortex is submitted to a periodic potential has a dramatic effect on the dynamics of a vortex dipole made of two counter-rotating parallel vortices; instead of rigidly translating as in the SFP, the vortex and antivortex approach each other by a series of jumps from one site to another until they annihilate in a very short time and their energy is transferred to bulk excitations.

I. INTRODUCTION

Vortices are characteristic quantized topological excitations of a superfluid. In the case of a Bose superfluid, a vortex represents a line singularity in the phase of the condensate wave function, with the phase having an increment of 2π as one turns around this line. Vortices in superfluid ^{4}He [1,2] and in cold bosonic atoms [3,4] have been extensively studied over the years, both as an example of the ubiquitous vorticity phenomena in many-body systems as well as a signature of the presence of phase coherence in the system. Vortices are expected to also be present in a supersolid.

The supersolid phase (SSP) of matter has attracted considerable interest because the two symmetries that are spontaneously broken at the same time seem incompatible at first sight [5]. On the one hand, the translational symmetry is broken so that particles localize with crystalline order. On the other hand, gauge symmetry is broken and this leads to a condensate and to the appearance of superfluid properties.

Supersolidity was proposed long ago for solid ^{4}He [6–8]. However, experiments have shown that low-temperature (*T*) solid ^{4}He, in spite of displaying a number of anomalous properties, does not conform to the bulk supersolid paradigm [9,10]. Cold bosons have turned out to be a more fruitful platform to address supersolidity. As discussed in the following, a number of properties expected for a supersolid have recently been verified for systems made of bosonic atoms with a permanent magnetic moment (dipolar bosons).

One should expect differences between the appearance and dynamics of a vortex in a superfluid and in a supersolid due to

its completely different environment. In a superfluid, density can be nonuniform, e.g., close to an interface or in the whole volume as for cold atoms in a trap. These are large-scale inhomogeneities compared to the vortex core radius, and the vortex is free to move inside the superfluid, which it sees as locally uniform. This behavior is similar to that of vortices in classical hydrodynamics: vortices are free to move inside the fluid and each vortex moves with the local velocity due to the presence of other vortices [11]. The density in a supersolid has a strong spatial modulation on the microscopic scale. Since, in order to minimize its kinetic energy, a vortex is a low density "seeker," it is no longer free to move as in the superfluid phase (SFP). Rather, it behaves as if it were moving in a periodic potential with a spatial scale comparable to its core size. In addition, this density inhomogeneity is not simply due to an external potential, but the interparticle interactions play a key role in establishing it. This is quite a different regime and the main purpose of the present paper is to uncover and discuss some of its properties.

Experiments, in agreement with the predictions of theory, show that dipolar bosons can be found in different phases. When the dipole interaction strength is small, the system is in the superfluid phase. As the interaction strength increases, the dipolar boson dispersion relation [excitation energy as a function of the momentum of the excitation, $\mathcal{E}(k)$] displays a roton minimum whose gap amplitude depends on the relative strengths of short-range and dipolar interactions [12,13]. Such dispersion relation has some similarities with that of superfluid ^{4}He [1,4]. When the ratio of the dipolar to the short-range interaction increases beyond a critical value, a

033314-1

spontaneous density modulation occurs which is driven by the softening of the roton mode at finite momentum k_R, and the resulting system has supersolid character [12,14–18]. The density modulation, with wavelength $\sim 2\pi/k_R$, results in an ordered array of "droplets," made of many atoms each, elongated in the direction of the polarization axis. Global phase coherence is maintained between adjacent droplets due to a low-density superfluid background that allows atom tunneling from one superfluid droplet to another. As the ratio between interactions is further increased, the superfluid background almost disappears so that phase coherence is no longer present between droplets, and the phase becomes a "normal solid phase" (NSP), even if each droplet can be superfluid.

Further increase of that ratio eventually results in a transition to a totally different regime, characterized by the formation of *self-bound* droplets [19–24], with order-of-magnitude higher densities, and with the binding arising from the interplay between the two-body dipolar interactions and the effect of quantum fluctuations [22,25].

In dipolar bosons, supersolid behavior occurs in the intermediate regime between superfluid and self-bound droplet regimes. We remark that the term droplet will be used here to indicate the individual clusters making up the ordered structure of a modulated phase in such intermediate regime, and will not refer to the self-bound droplet regime.

A number of theoretical studies predicted supersolid behavior in dipolar Bose-Einstein condensates (BEC) in different geometries [14,26,27], dipolar gases confined in a quasi-2D pancake-shaped trap [15,23], or in a tube [18]. The order of the superfluid-supersolid transition has been studied in Ref. [28].

Experiments provide evidence of SSP in dipolar bosons in a number of ways. Strong global phase coherence was found in the SSP realization of Ref. [29] as opposed to the lack of it in the isolated droplet phase where no superfluid flow is present between adjacent droplets in the NSP. Similarly, robust phase coherence across a linear array of quantum droplets was observed in Ref. [30]. Stable stripe modulations have also been observed in dipolar quantum gases [14,31]. A partial phase coherence is suggested in Ref. [31], thus indicating possible SSP behavior. The characteristic symmetry breaking of a SSP was observed through the appearance of compressional oscillation modes in a harmonically trapped dipolar condensate [32]. In another work [33], the reduction of the moment of inertia under slow rotation—previously predicted for a dipolar SSP [34]—was measured. The response of the dipolar SSP has been studied experimentally in Ref. [35], where the out-of-equilibrium superfluid flow across the whole system was revealed by a rapid reestablishment of global phase coherence after a phase-shattering excitation was applied. Instead, no such rephasing was observed in the NSP, where tunneling between adjacent droplets is suppressed.

Most of the recent evidence of supersolid behavior in dipolar gases is based on the identification of two main features of a SSP, i.e., (i) a nonzero, nonclassical translational and rotational inertia [36] and (ii) the appearance of the Nambu-Goldstone gapless mode [37] corresponding to phase fluctuations—besides the phonon mode associated to density fluctuations which results from the translational discrete symmetry of the system. But no evidence of another hallmark of superfluidity has been gathered so far, namely, the presence of quantized vortices [34]. Experimental realization and detection of quantized vortices would provide a direct evidence of global coherence in the SSP of a dipolar system.

The structure of vortex arrays in a trapped supersolid system rotating in the plane orthogonal to the polarization axis has been theoretically studied in Ref. [38], where vortex nucleation was found to be triggered, as in standard condensates, by the softening of the surface quadrupole mode. For larger values of the angular velocity of the rotating trap, an array of regularly arranged vortices appears, which coexists with the triangular geometry of the supersolid lattice and persists during the free expansion of the atomic cloud. The vortex cores are localized in the interstitial regions between droplets, where the local particle density can be very small. As a consequence, the critical angular velocity for the nucleation of an energetically stable vortex in the SSP has been found to decrease with respect to that in the SFP [38]. It was shown in Ref. [39] that a vortex-hosting trapped SSP could be obtained by starting from the vortex-hosting superfluid phase and tuning the interaction strength to that of the SSP. There it was also shown that evidence for the presence of vortices in the SSP could be obtained from interference features of the expanding cloud.

Previous theoretical studies of vortices in a SSP have been performed for dipolar bosons in full confinement in a rotating trap, i.e., in a harmonic trap along the three spatial directions. In order to achieve an understanding of the intrinsic properties of a vortex in the SSP, in the present work we study isolated vortices in the SSP of an extended dipolar BEC, i.e., free from the radial harmonic trap in the plane perpendicular to the polarization direction, but subject to a harmonic confinement along it. The use of periodic boundary conditions in the plane dictates that the crystalline structure of the SSP is fixed in space and vortices are imprinted by suitable phase factors. We find that a single vortex is a stable excitations of the system.

We compare the properties of a vortex in the SFP of dipolar bosons with those in the SSP and study how the vortex energy changes depending on the location of the vortex core in the droplet network. We find that a vortex dipole, i.e., two vortices of opposite chirality, has a completely different behavior in the SSP than in the SFP. A vortex dipole in the SFP uniformly translates, keeping a fixed intervortex distance unless the two vortices are very close at distances of order of the healing length [1,40]. At variance, as a consequence of the spatial modulation of the condensate, we find that in the SSP, the dipole does not translate and it is no longer a stable excitation of the system; rather, the two vortices of opposite chirality feel an attractive interaction so that they approach each other until they annihilate each other and their energy is transferred into bulk excitations.

This paper is organized as follows. In Sec. II, we present the theoretical model and outline the numerical methods used in this study. The ground state of dipolar bosons in the SFP and in the SSP is studied in Sec. III. We present the results for a single vortex in Sec. IV and discuss the results for a vortex dipole in Sec. V. Finally, Sec. VI contains a summary of our study.

II. METHOD

A standard approximation for dipolar bosonic atoms with mass m and magnetic moment μ at $T = 0$ is represented by a macroscopic wave function $\phi(\mathbf{r})$ that obeys the extended Gross-Pitaevskii equation (eGPE) [22]:

$$H\phi(\mathbf{r}) \equiv \left\{ -\frac{\hbar^2}{2m}\nabla^2 + V_t(\mathbf{r}) + g|\phi(\mathbf{r})|^2 + \gamma(\epsilon_{dd})|\phi(\mathbf{r})|^3 \right.$$
$$\left. + \int d\mathbf{r}'|\phi(\mathbf{r}')|^2 V_{dd}(\mathbf{r} - \mathbf{r}') \right\}\phi(\mathbf{r}) = \varepsilon\phi(\mathbf{r}). \quad (1)$$

Here, $g = 4\pi\hbar^2 a_s/m$, where a_s is the s-wave scattering length, $V_{dd}(\mathbf{r}) = \frac{\mu_0\mu^2}{4\pi}\frac{1-3\cos^2\theta}{r^3}$ is the dipole-dipole interaction between two identical magnetic dipoles aligned along the z axis (θ being the angle between the vector $\mathbf{r}$ and the polarization direction z), and μ_0 is the permeability of the vacuum. $V_t(\mathbf{r})$ is the trapping potential. The number density of the system is $\rho(\mathbf{r}) = |\phi(\mathbf{r})|^2$. The $\gamma(\epsilon_{dd})$ term is the beyond-mean-field [Lee-Huang-Yang, (LHY)] correction [25], where $\gamma(\epsilon_{dd}) = \frac{32}{3\sqrt{\pi}}ga_s^{3/2}F(\epsilon_{dd})$, with $\epsilon_{dd} = \frac{\mu_0\mu^2}{3g}$ being the ratio between the strengths of the dipole-dipole and contact interactions, and $F(\epsilon_{dd}) = \frac{1}{2}\int_0^\pi d\theta \sin\theta[1 + \epsilon_{dd}(3\cos^2\theta - 1)]^{5/2}$. The chemical potential ε is determined by the normalization condition $\int |\phi(\mathbf{r})|^2 d\mathbf{r} = N$, with N being the total number of dipoles.

We solve the above equation by propagating it in imaginary time, if stationary states are sought, or by propagating in real time its time-dependent counterpart $i\hbar\partial\phi/\partial t = H\phi$ to simulate the dynamics of the system, starting from a suitable initial wave function specified in the following sections.

To compute the spatial derivatives appearing in Eq. (1), we used an accurate 13-point finite-difference formula [41]. The convolution integral in the potential-energy term of Eq. (1) is efficiently evaluated in reciprocal space by using fast Fourier transforms, recalling that the Fourier transform of the dipolar interaction is $\tilde{V}_{\mathbf{k}} = (\mu_0\mu/3)(3\cos^2\alpha - 1)$, where α is the angle between $\mathbf{k}$ and the z axis [42]. The spatial mesh spacing and time step are chosen such that during the time evolution, excellent conservation of the total energy of the system is guaranteed. We verified that the dimension of the simulation cell along the z direction, where the harmonic confinement is active, is wide enough to make negligible the effect, on the energy values and density profiles, of the dipole-dipole interaction between periodically repeated images.

The investigated system is made by $N \sim 1.3$–1.4×10^6 ^{164}Dy atoms (the chosen N value slightly changes depending upon the value of a_s, as discussed in the following), subject to a harmonic trapping potential along the z axis, with frequency $\omega_z = 150 \times 2\pi$ Hz. The harmonic length associated to this trapping potential is $a_{ho} = \sqrt{\hbar^2/m\omega_z} = 1.2112 \times 10^4 a_0 = 0.64$ μm. The dipolar gas is thus extended in the x-y plane (with periodic boundary conditions) and flattened in the direction of the dipole polarization. Typical transverse sizes are $L_x, L_y \sim 30$ μm.

A linear, singly quantized vortex excitation in the extended dipolar system with axis in the z direction and core in the position (x_v, y_v) can be generated by the "imprinting procedure" [41], i.e., we compute the lowest-energy state obtained by

starting the imaginary-time evolution from the wave function,

$$\phi_0(\mathbf{r}) = \rho_0^{1/2}(\mathbf{r})\left[\frac{(x-x_v) + \iota(y-y_v)}{\sqrt{(x-x_v)^2 + (y-y_v)^2}}\right], \quad (2)$$

where $\rho_0(\mathbf{r})$ is the ground-state density of the vortex-free dipolar system. During the imaginary-time evolution, the vortex position and vortex core structure change to provide, at convergence, the lowest-energy configuration.

The flow field of a linear vortex has a long-range character, $\sim 1/r$, where r is the distance from the vortex axis. We have imposed antiperiodic boundary conditions [43] in order that the condition of no flow across the boundary of the computational cell is satisfied. This is equivalent to sum over the phases of an infinite array of vortex-antivortex, i.e., a vortex of opposite chirality is present in each nearest-neighbor cell of the computation cell [44]. The sign of the circulation can be changed by changing the sign of the complex ι in Eq. (2); this equation can be easily generalized to accommodate a vortex array made of an arbitrary number of vortices and/or antivortices [45]. A generalization to the case of a pair of vortices with opposite circulation (vortex dipole) will be used in Sec. V.

III. GROUND STATE IN DIPOLAR BOSONS

We have taken, as a case study, a dipolar bosons system made of ^{164}Dy atoms. The relative strength of the dipolar interaction over the short-range one is defined by the dimensionless parameter $\epsilon_{dd} = a_{dd}/a_s$, where $a_{dd} = 132 a_0$ is the dipolar length for ^{164}Dy atoms [35]. The behavior of dipolar bosons crucially depends on the value of the ϵ_{dd} ratio, whose value can be experimentally varied by changing a_s.

When ϵ_{dd} is below a threshold value ϵ_{dd}^c, the system at $T = 0$ K is in a standard superfluid state; in our case, it is uniform in the x-y plane and nonuniform in the z direction due to the trap in that direction. When ϵ_{dd} is above the threshold, the system spontaneously develops a periodic density modulation in the x-y plane, entering the SSP.

As ϵ_{dd} is increased toward the threshold, one can get a signature of the SFP to SSP transition from the excitation spectrum of the superfluid, $\mathcal{E}(k)$. We first obtain the ground-state SFP wave function by propagating, in imaginary time, a starting wave function which is just a constant in the x, y variables times the ground-state wave function for free particles in the $V_t(z)$ trap. Next, using the method described in Ref. [18], we solve the Bogoliubov–de Gennes equations for superfluid states corresponding to different ϵ_{dd} values. For small ϵ_{dd}, the dispersion relation $\mathcal{E}(k)$ is structureless, starting as a linear function of k corresponding to phonon excitations, which evolves toward a quadratic dispersion at large k corresponding to free particles. Increasing ϵ_{dd}, the excitation spectrum changes shape and, close to ϵ_{dd}^c, $\mathcal{E}(k)$ develops a phonon-maxon-roton structure, as shown in Fig. 1. This is due to the interplay between confinement in the z direction and the interatomic interaction consisting of the short-range interaction plus the long-range interaction of the dipoles oriented in the direction of the confinement [12,13].

The four curves in Fig. 1 show the excitation spectrum of the SFP for $a_s = 97.8, 98, 98.5,$ and $99 a_0$, which correspond to a narrow range of ϵ_{dd} values between $\epsilon_{dd} = 1.35$
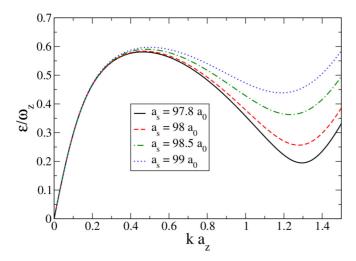
FIG. 1. Dispersion relation $\mathcal{E}(k)$ of the extended SFP as a function of the wave vector k in the x-y plane for different values of a_s. $\mathcal{E}(k)$ is in units of the harmonic energy ω_z and k is in units of the inverse of the harmonic length, $a_{ho} = \sqrt{\hbar/(m\omega_z)}$.

FIG. 2. Supersolid phase for the extended system with $a_s = 93 \, a_0$. Upper panel: number density ρ in a x-z plane passing through a row of droplets, in units of a_{ho}^{-3}. Lower panel: integrated density along the z direction, shown in the x-y plane, in units of a_{ho}^{-2}. The lengths along the axis are in μm.

(corresponding to $a_s = 97.8 \, a_0$) and $\epsilon_{dd} = 1.33$ (corresponding to $a_s = 99 \, a_0$). The vanishing of the roton gap in the present case occurs just below $a_s = 97.8 \, a_0$, corresponding to the value $\epsilon_{dd}^c \sim 1.35$. Notice that this value depends on the strength of confinement in the z direction and on the mass of the bosons. Beyond the threshold, the system becomes nonuniform in the x and y directions.

We obtain the ground-state wave function in the SSP by evolving, in imaginary time, a starting wave function that is a superposition of Gaussian profiles in the x-y plane, located at the sites of a triangular lattice, modulated along the z direction by the ground state of free particles in the harmonic trap in that direction. In the following, most results are obtained with ϵ_{dd} in the $1.39 < \epsilon_{dd} < 1.48$ range, where the system shows spontaneous density modulation with supersolid behavior. The scattering lengths associated to this interval are $95 \, a_0 > a_s > 89 \, a_0$.

The modulated system obtained in this way consists of a planar ordered array of "droplets" with triangular symmetry, elongated in the direction of the polarization axis, each containing $\sim 15\,000$ atoms. To good approximation, these cigar-shaped droplets are circular in the x-y plane and with an extension in the z direction, which is typically 4–5 times larger than their diameter in the x-y plane, as shown in Fig. 2 for $a_s = 93 \, a_0$.

An almost uniform fluid occupies the space between droplets, and its density is much smaller than that of the droplets. Global phase coherence is maintained between adjacent droplets due to this low-density superfluid background, which allows tunneling of atoms from one droplet to another. Typical average densities in the $z = 0$ plane of symmetry are $\rho_{av} \sim 3.5 \times 10^{-11} \, a_0^{-3}$.

The triangular packing of droplets is characterized by a lattice constant a, corresponding to the nearest-neighbor distance between two adjacent droplets. The periodic boundary conditions impose a constraint on the value of a such that an integer number of crystalline cells fits in the size of the computation box. For a given value of the scattering length
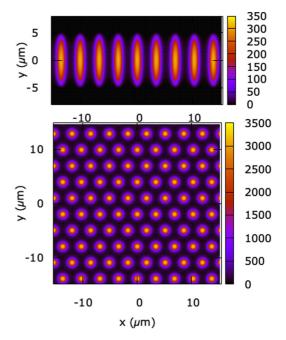
a_s, we preliminarily determine the equilibrium value for a by computing the energy per atom for different values of a and look for the minimum-energy value. An example of such calculation is shown in Fig. 3, where the energy per atom is shown—for the $a_s = 93 \, a_0$ case—as a function of the lattice constant a. As a result, the total number N of atoms depends on the value of a_s, and N changes by about 8% in the range of scattering length considered in our work. Figure 4 shows the equilibrium values of the lattice constant for different choices of a_s.

All the modulated structures investigated here have supersolid character. In order to prove this, we checked for the presence of a finite nonclassical translational inertia (NCTI) in the system. This is done by solving, for stationary states, the real-time version of Eq. (1) in the comoving reference frame
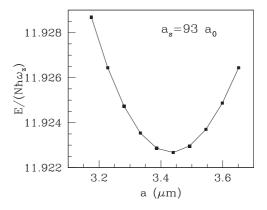

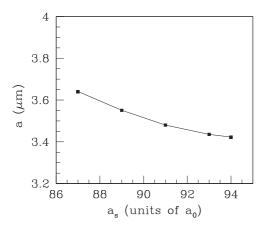FIG. 3. Energy per atom vs a for the case $a_s = 93 \, a_0$.

FIG. 4. Equilibrium value of the lattice constant a as a function of the scattering length a_s.

with uniform velocity v_x, i.e.,

$$i\hbar \frac{\partial}{\partial t}\phi(\mathbf{r}) = \left(H + i\hbar v_x \frac{\partial}{\partial x}\right)\phi(\mathbf{r}). \qquad (3)$$

Following Ref. [36], we define the superfluid fraction f_s as the fraction of particles that remains at rest in the comoving frame,

$$f_s = 1 - \lim_{v_x \to 0} \frac{\langle P_x \rangle}{Nmv_x}, \qquad (4)$$

where $\langle P_x \rangle = -i\hbar \int d\mathbf{r}\, \phi^* \partial\phi/\partial x$ is the expectation value of the momentum and Nmv_x is the total momentum of the system if all atoms were moving. We have verified that in the low-velocity limit, the same value for f_s is obtained by instead applying the boost along the y direction. We remark that the superfluid fraction computed in this way should not be confused with the total superfluid fraction because each droplet is superfluid, but does not necessarily contribute to the superfluid response of the overall system.

The calculated average superfluid fraction is shown in Fig. 5 as a function of a_s. We also show in the same figure the ratio between the density $\rho_{\min}$ of the superfluid background
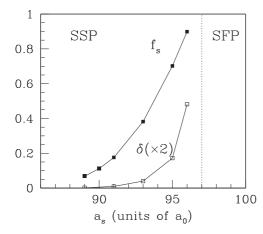

FIG. 5. Upper curve: superfluid fraction f_s. Lower curve: ratio $\delta = \rho_{\min}/\rho_{\max}$. The vertical line shows the location of the SFP → SSP transition.
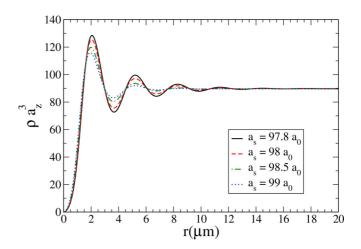

FIG. 6. Radial vortex density profiles in the SFP for different a_s values.

in the interstitial site between three adjacent droplets and the maximum density of the clusters in the $z = 0$ plane of symmetry, $\delta = \rho_{\min}/\rho_{\max}$. Not surprisingly, the lower the ratio, the smaller the associated superfluid fraction. We find that the SFP → SSP transition occurs around the value $a_s = 97\, a_0$ (an exact determination from the simulation is problematic: close to the transition residual, very low modulations in the density take overly long imaginary times to be reduced). The vertical line in Fig. 5 shows the estimated location of the SFP → SSP transition. For values of a_s to the right of this line, the lowest-energy structure is a homogeneous (in the x-y plane) SFP with $f_s = 1$.

In the SSP regime, when the value of a_s is progressively decreased, the background density becomes steadily smaller and eventually the system is no longer supersolid, being composed of isolated droplets with incoherent phases [29]. We cannot follow this transition from a supersolid to this "normal solid" made of droplets (the NSP in our notation) because the theory that we use, which is based on a single order parameter implying a global phase coherence across the whole system, is not fully appropriate when the different droplets become incoherent.

IV. SINGLE VORTEX IN DIPOLAR BOSONS

We have studied singly quantized vortices in our extended system for different values of the scattering length a_s. In the SFP, the density profile is featureless for large a_s values, quadratically vanishing at the position of the vortex core and monotonously approaching the bulk density at large distances, as in usual BEC systems. As a_s is decreased (and thus ϵ_{dd} increases), the density profile develops damped oscillations near the vortex core [46]. This is shown in Fig. 6, where we display the equilibrium vortex-hosting density profiles in the SFP for the same a_s values as in Fig. 1. The smaller the a_s, the higher the density peaks around the vortex core. The oscillations become more pronounced as the instability limit $\epsilon_{dd}^c \sim 1.35$ is approached. The wave vector of the oscillations in the vortex-hosting density profile is close to the roton k_R. These oscillations are similar to those predicted in superfluid
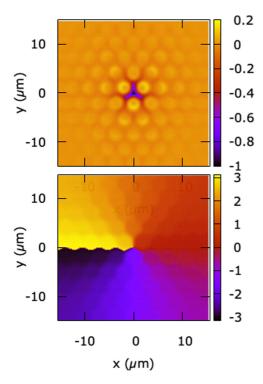
FIG. 7. Upper panel: Density difference ($\rho_{\text{vortex}} - \rho_{\text{no vortex}})/\rho_{\text{no vortex}}$ in the $z = 0$ symmetry plane for the vortex at the interstitial site when $a_s = 93\, a_0$. Lengths are in μm. Lower panel: Phase (in radians) of the vortex state shown in the upper panel. The lengths along the axis are in μm.

⁴He, which have been described as a cloud of virtual rotons [47].

As we have discussed previously, when a_s becomes smaller than a critical value, the system enters the supersolid phase, as in the structure shown in Fig. 2. In this phase, the lowest-energy position of the vortex core is in the interstitial region between three adjacent droplets, where the local particle density $\rho(\mathbf{r})$ is very small, so that the energy cost of the additional depression of $\rho(\mathbf{r})$ near the vortex core (remember that the local density has to vanish at the vortex core) is minimized and the kinetic energy of the superfluid flow around the vortex core also decreases [34]. To visualize the vortex-core structure, the map of the difference between the densities of the configuration with and without vortex at the interstitial site for the $a_s = 93\, a_0$ case is shown in the upper panel of Fig. 7. It appears that the core is very deformed following the symmetry of the interstitial site [34]. We have found a similar vortex-core structure for other values of the scattering length.

The phase associated to the vortex is shown in the lower panel of Fig. 7. Notice the hexagonal texture, which is a consequence of the triangular lattice of clusters in the vortex-hosting SSP. As shown in Fig. 8, this texture becomes prominent in the plot of the modulus of the velocity field $|\mathbf{v}(\mathbf{r})|$, where $\mathbf{v}(\mathbf{r}) = (\hbar/m)\nabla_R \theta(\mathbf{r})$, with θ being the phase of the order parameter ϕ, and $\nabla_R \equiv (\partial/\partial x, \partial/\partial y)$. It appears that $|\mathbf{v}(\mathbf{r})|$ completely differs from the $1/r$ behavior in a superfluid, being instead strongly anisotropic and modulated, and very small inside the droplets. We will show below how this is affecting the kinetic energy of the vortex.
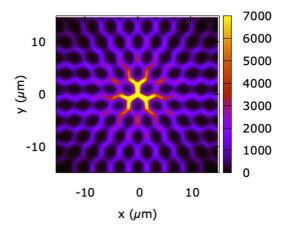

FIG. 8. Modulus of the velocity field (in units of $a_0\omega_z$) on the $z = 0$ plane of symmetry for $a_s = 93\, a_0$. The lengths along the axis are in μm.

We show in Fig. 9 the velocity streamlines in the $z = 0$ symmetry plane for the case described above, which are remarkably different from the simple tangential flow of a vortex in a homogeneous superfluid. We find that the circulation calculated around a closed path encircling the vortex core is $\oint \mathbf{v} \cdot \mathbf{dl} = (2\pi\hbar/m)n$, with $n = 1.01 \pm 0.01$, and where the error reflects slightly different outcomes depending on the chosen size of the closed path around the vortex core.

Besides the stable equilibrium vortex position at interstitial sites of the triangular droplet lattice, we have found that the saddle point between two adjacent droplets is a (meta)stable equilibrium vortex position, with slightly higher energy than the interstitial equilibrium one. The map of the difference between the densities of the configuration with and without vortex at the saddle point for the $a_s = 93\, a_0$ case is shown in Fig. 10. Again, the density depression due to the vortex is very anisotropic and reflects the local symmetry of the system.

We also considered the possibility of a third equilibrium position with the vortex line piercing a droplet parallel to the
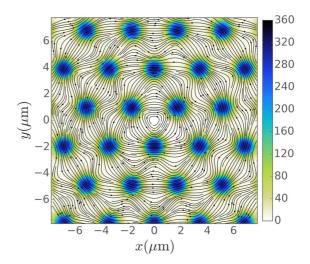

FIG. 9. Velocity streamlines for the SFP state for $a_s = 93\, a_0$. The vortex core is in the origin. Superimposed to the field lines is the density in the $z = 0$ plane, in units of a_{ho}^{-3}.
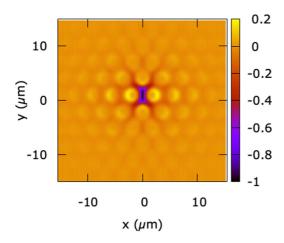
FIG. 10. Density difference $(\rho_{\text{vortex}} - \rho_{\text{no vortex}})/\rho_{\text{no vortex}}$ in the $z = 0$ symmetry plane for the vortex at the saddle-point site when $a_s = 93 \, a_0$. The lengths along the axis are in μm.

polarization axis and passing through its center. Such configuration has proven, however, to be unstable, and the vortex line is expelled during the imaginary-time minimization, ending in the lowest-energy interstitial site configuration. A similar unstable behavior has been observed for a vortex aligned with the polarization axis at the center of self-bound dipolar droplets [48].

The difference between the energies of the saddle-point and interstitial site configurations represents the barrier for displacing a vortex through the supersolid lattice. The calculated energy barriers per unit length are shown in Fig. 11 for different values of a_s. Here, L is the length of the vortex line along the z direction, which we take as $L = \sqrt{\int \bar{\rho}(z)z^2 dz / \int \bar{\rho}(z)dz}$, where $\bar{\rho}(z) \equiv \int \rho(x, y, z)dxdy/(L_x L_y)$. We find $L \sim 6.7 \, \mu$m. We notice the strong decrease of the energy barrier as the density of the superfluid background diminishes.

Although the very deformed and anisotropic shape of the vortex core in the SSP as shown in Fig. 7 hinders a clear definition of the vortex-core extension, one can estimate it by performing an angular average of the density (on the $z = 0$
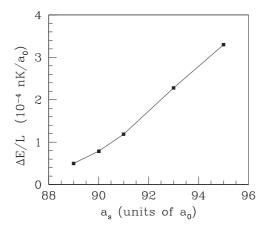

FIG. 11. Energy barrier per unit length in the z direction between interstitial and saddle-point configurations as a function of a_s.
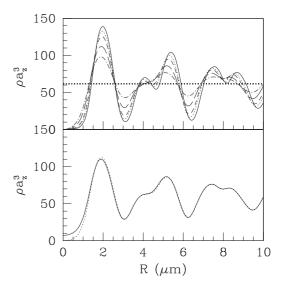

FIG. 12. Upper panel: angular average on the $z = 0$ symmetry plane, of the number density around a vortex. From top to bottom—at the first maximum—$a_s = 89, 90, 91, 93,$ and $95 \, a_0$. The nearly overlapping horizontal lines show the average densities on the same plane. Lower panel: angular average of the number density with and without vortex, for the $a_s = 93 \, a_0$ case.

symmetry plane) over the polar angle around the interstitial site where the vortex is placed. We show this average in the lower panel of Fig. 12 for the state with and without vortex corresponding to $a_s = 93 \, a_0$; the upper panel shows such angular average for different values of a_s. The horizontal lines show, in the same $z = 0$ symmetry plane, the density values obtained by additional averaging over the radial distance, for the same a_s values. The radius R_c of the averaged cavity is measured at half the value of the depression of the local density at the vortex axis, i.e., from the condition $\rho_0(R_c) - \rho_v(R_c) = \rho_0(0)/2$, where ρ_v and ρ_0 are the average density profiles with and without vortex, respectively. The cavity radius so calculated ranges from $R_c \sim 23\,000 \, a_0$ for $a_s = 95 \, a_0$ to $R_c \sim 35\,000 \, a_0$ for $a_s = 89 \, a_0$. The calculated values are reported in Table I. For comparison, the distance between the vortex-core position and the neighboring droplets center is $37\,000 \, a_0$ (for the $a_s = 93 \, a_0$ case).

A measure of the local vortex excitation energy per unit length of a vortex of length L is the integrated vortex kinetic energy [47,49], which can be defined as follows:

$$\epsilon_v(R) = \frac{1}{L} \big[E_{\text{kin}}^v(R) - E_{\text{kin}}(R) \big], \tag{5}$$

where E_{kin}^v, E_{kin} are the kinetic energies within a cylinder of radius $R = \sqrt{x^2 + y^2}$ and length L (with and without a vortex line along its axis) as a function of the distance R from the vortex axis (here, the z axis).

Neglecting the z dependence of the energy, we compute $\epsilon_v(R)$ by averaging the kinetic-energy densities on the $z = 0$ symmetry plane. The kinetic energy per unit length is thus given by the integral

$$\frac{E_{\text{kin}}(R)}{L} = 2\pi \int_0^R \epsilon(R')R'dR', \tag{6}$$

TABLE I. Parameters ρ_0 and λ of the fit of the vortex kinetic energy with the hydrodynamic form given by Eq. (8) for some values of a_s in the superfluid (SFP) and in the supersolid (SSP). Other reported quantities are the average density ρ_{av} on the $z = 0$ plane, the density $\rho_{\min}$ at the interstitial site of the supersolid, the radius R_c of the vortex cavity, and the vortex core energy E_c.

a_s (a_0)	ρ_0 (a_0^{-3})	λ (a_0)	ρ_{av} (a_0^{-3})	$\rho_{\min}$ (a_0^{-3})	R_c (a_0)	E_c (nK/a_0)
89 (SSP)	1.23×10^{-11}	24 360	3.45×10^{-11}	4.36×10^{-13}	35 221	2.27×10^{-2}
90 (SSP)	1.82×10^{-11}	23 160	3.46×10^{-11}	7.97×10^{-13}	32 704	3.18×10^{-2}
91 (SSP)	2.56×10^{-11}	21 790	3.47×10^{-11}	1.40×10^{-12}	30 474	4.33×10^{-2}
93 (SSP)	4.56×10^{-11}	20 180	3.49×10^{-11}	4.01×10^{-12}	26 130	6.50×10^{-2}
95 (SSP)	6.44×10^{-11}	15 420	3.51×10^{-11}	1.09×10^{-11}	22 644	8.40×10^{-2}
98 (SFP)	3.54×10^{-11}	7484	3.53×10^{-11}		17 755	5.56×10^{-2}
100 (SFP)	3.52×10^{-11}	7777	3.52×10^{-11}		16 470	5.72×10^{-2}
105 (SFP)	3.50×10^{-11}	7612	3.50×10^{-11}		14 350	5.97×10^{-2}
110 (SFP)	3.48×10^{-11}	7200	3.48×10^{-11}		12 750	6.03×10^{-2}

where $\epsilon(R)$ is the angular average, performed in the $z = 0$ plane, of $(\hbar^2/2m)|\nabla_R \phi|^2$, where $\nabla_R \equiv (\partial/\partial x, \partial/\partial y)$. Similar expressions hold for $E_{\mathrm{kin}}^v(R)/L$.

We notice that the classical hydrodynamical counterpart of $\epsilon_v(R)$ for a vortex of circulation κ in an incompressible fluid of density ρ_0 is

$$\epsilon_v^{\mathrm{hydro}}(R) = \frac{\kappa^2}{4\pi} m \rho_0 \left[\ln\left(\frac{R}{d_v}\right) + \delta \right], \quad (7)$$

where d_v is the vortex-core radius and δ depends on the core model ($\delta = 0$ for the hollow core model and $\delta = 1/4$ for a core in rigid rotation) [1]. The parameter δ in the previous equation can be absorbed in the logarithmic term; using the quantum value for the circulation, $\kappa = h/m$, for a singly quantized vortex $\epsilon_v^{\mathrm{hydro}}$ reads

$$\epsilon_v^{\mathrm{hydro}}(R) = \frac{\hbar^2}{m} \pi \rho_0 \, \ln\left(\frac{R}{\lambda}\right), \quad (8)$$

where $\lambda = d_v e^{-\delta}$ is the core parameter.

We have used the above expression to fit the calculated $\epsilon_v(R)$ for the supersolid structures investigated here with fitting parameters ρ_0 and λ. We show in Fig. 13, for different values of a_s, the calculated $\epsilon_v(R)$ values (filled squares) and the best fit obtained by using the hydrodynamical approximation given by Eq. (8) (solid line). As expected, the
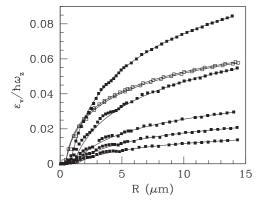

FIG. 13. Integrated vortex kinetic energy $E_v(R)$ as a function of the distance from the vortex core. Filled squares, from top to bottom: $a_s = 95, 93, 91, 90, 89\ a_0$ (SSP). Open squares: $a_s = 110, 100\ a_0$ (SFP). The lines are the hydrodynamical form fit.

approximation breaks down at distances approaching the vortex core, as there the local density becomes very small. One can notice from the figure that the computed kinetic energy has some weak oscillations whose locations are related to the distances from the interstitial site, where the vortex is placed, to the different droplet shells. For comparison, we also show in Fig. 13 the results for the vortex-hosting SFP corresponding to two a_s values (open squares). Notice that the supersolid vortex kinetic energy at $a_s = 95\ a_0$ has a higher value than in the superfluid phase. We do not have a simple explanation for this jump. The vortex kinetic energy in the supersolid differs from that in the superfluid for the very different character of the density profile and for a flow pattern much different from the tangential flow of the superfluid. We have not tried to disentangle the two effects.

We report in Table I the calculated values for the core parameter λ and prefactor ρ_0 as obtained from the fit. At variance with the SFP, for which the calculated value of ρ_0 coincides with the average density on the $z = 0$ plane (fourth column in the table), it does not for the SSP: here the calculated ρ_0 values show a marked decrease with a_s. One may argue that these values should be related to the superfluid halo embedding the droplets, and thus to the (minimum) density in the interstitial regions between droplets (fifth column in the table): this is not the case though since the minimum density values decrease with a_s much faster than ρ_0. We also show in the table the vortex "core" energy, defined as $E_v(R_c)$, where the core radius R_c has been estimated as described before.

The core parameter λ and core energy E_c depend only weakly on the density in the SFP, whereas the core radius R_c increases as a_s decreases, i.e., as the dipolar interaction becomes more important. In the SSP, there is a clear change in the dependence of these vortex parameters as a function of a_s. As mentioned before, ρ_0 is a strongly decreasing function of a_s. Both λ and R_c increase significantly for decreasing a_s, and this means that the vortex size expands as the value of the low-density halo decreases. The core energy has the opposite dependence on a_s, i.e., E_c decreases as a_s does, indicating that the decrease of the halo density has a stronger effect on the E_c value than the increase of the vortex-core radius.

An important issue is the nature of the low-energy excitations of a vortex in the SSP. We already mentioned a difference between a vortex in a superfluid and in a supersolid: in a homogeneous superfluid, a vortex can move without restriction

and its low-energy excitations are Kelvin waves whose energy in an unbounded fluid vanishes as the wave vector k goes to zero [1,11]. We have shown that in a supersolid, a vortex has a discrete set of equilibrium positions and an energy barrier is present for its motion from one site to another. Therefore, the vortex is a localized excitation in the plane perpendicular to the vortex axis and this should modify the properties of the Kelvin waves. In particular, their spectrum should display an energy gap because the vanishing of the spectrum of the Kelvin waves in the limit of zero wave vector is a consequence of the translational invariance of the vortex excitation in a uniform superfluid, invariance that is absent in the supersolid. This predicted gap in the supersolid has a completely different origin from the small energy gap of Kelvin waves when bosons are in a trap [50].

There is the possibility that the low-energy excitations of a vortex in a supersolid have a quite different character when the droplets are very elongated along the z axis. Such excitations could be kinks along the vortex axis such that the vortex core moves from one equilibrium site to another site along the axis. The energy of the vortex in a SSP is a periodic function of position and this plays a role similar to the Peierls potential acting on a dislocation in a crystalline solid. Kinks are indeed the low-energy excitations of a dislocation in solid ⁴He [51]. The study of the excitations of a vortex in a supersolid is an interesting problem, but it is quite outside the scope of the present paper.

V. VORTEX DIPOLE IN DIPOLAR BOSONS

As discussed in Sec. IV, vortices in a dipolar supersolid have well-defined equilibrium positions in the "solid" structure so that the vortex energy is a periodic function of its position. Therefore, a number of properties are expected to differ from those in a superfluid. In this section, we study one of them, namely, the dynamics of a vortex dipole, i.e., two counter-rotating straight parallel vortices. Vortex dipoles have been created and observed in BECs confined by parabolic potentials [52], and the motion of vortex dipoles in superfluid ⁴He has been simulated within the time-dependent density functional theory (DFT) approach [53].

In classical hydrodynamics of incompressible fluids [11], a vortex dipole is a stable entity that moves with a constant velocity that is perpendicular to the plane containing the vortices and inversely proportional to the distance d between them. The same behavior holds in superfluid systems when d is much larger than the healing length (which, in the present case, can be estimated from the vortex-core sizes in Fig. 6); in the superfluid, the vortex dipole propagates with a constant velocity $v_d = \hbar/(m\,d)$ [1].

We have addressed the dynamics of a vortex dipole in the extended dipolar bosons system. To this end, we have first prepared the initial vortex dipole configuration. This can be done generalizing Eq. (2) in Sec. II as follows:

$$\phi_0(\mathbf{r}) = \rho_0^{1/2}(\mathbf{r})\left[\frac{(x - x_v) + \iota(y - y_v)}{\sqrt{(x - x_v)^2 + (y - y_v)^2}}\right.$$
$$\left.\times \frac{(x - x_{\bar{v}}) - \iota(y - y_{\bar{v}})}{\sqrt{(x - x_{\bar{v}})^2 + (y - y_{\bar{v}})^2}}\right], \quad (9)$$
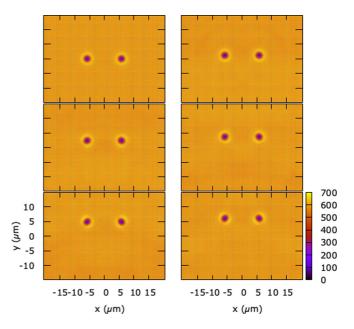

FIG. 14. Vortex-antivortex dynamics in real time, for the case $a_s = 110\,a_0$ (SFP). The density, integrated along the z axis, is shown in units of a_{ho}^{-2}. Snapshots are taken, from top to bottom and from left to right, at $t = 0, 24, 48, 72, 96$, and 120 ms. Lengths are in μm.

where $(x_v, y_v) = (d/2, 0)$ and $(x_{\bar{v}}, y_{\bar{v}}) = (-d/2, 0)$. We evolve this wave function in imaginary time until a stationary configuration is reached. Since the total circulation is zero, usual periodic boundary conditions can be used.

It should be noticed that the dipole wave function is not orthogonal to that of the ground state. Hence, a very long imaginary-time evolution would bring the initial state $\phi_0(\mathbf{r})$ to the ground state of the system, i.e., the vortex dipole would disappear. However, we find that after a relatively short imaginary time τ_c, the initial phase settles down to a quasistationary state where the vortex cores are fully developed while remaining in their initial positions (whereas orders-of-magnitude longer imaginary times would be needed to recover the vortex-free ground state). At this point, we initiate the evolution of the wave function in real time. By using different values of τ_c, we have verified that the real-time evolution does not depend on the used τ_c value.

We have first studied the vortex dipole in the SFP. In this case, we find that the vortex dipole translates with a constant velocity, and this velocity is of the order of that given by classical hydrodynamics, $v_d = \hbar/(m\,d)$. Notice that the observed velocity can differ from the hydrodynamic result for two reasons: because d is not very large compared to the healing length and because the periodic boundary conditions modify the streamlines of the dipole near the cell boundaries with respect to those in an unbounded fluid [40].

The real-time evolution of a vortex dipole in the SFP for $a_s = 110\,a_0$ is shown in Fig. 14, in the form of snapshots of the density taken at increasing times during the dynamics. The vortex dipole has been prepared with an initial vortex-antivortex distance $d = 6.5\,\mu$m.

A completely different behavior is found in the SSP: no translation of the dipole takes place, and the two vortices approach until they annihilate each other. The dynamics of
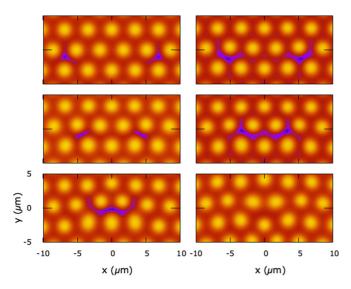
FIG. 15. Vortex-antivortex dynamics in real time, for the case $a_s = 93\ a_0$ (SSP). For clarity, the logarithm of the z-averaged density (in units of a_{ho}^{-2}) is shown. Snapshots are taken, from top to bottom and from left to right, at $t = 0, 27, 36, 41, 48$, and 75 ms. Lengths are in μm.

FIG. 16. Energy spectrum (in units of 1×10^{-18} hartree $\times a_0$) before (top) and after (bottom) the vortex dipole annihilation in the SSP with $a_s = 93\ a_0$. Solid lines: incompressible spectrum; dashed lines: compressible spectrum. The meaning of the vertical lines is explained in the text.

a vortex dipole in the SSP is displayed in Fig. 15, where it appears that the vortex-antivortex pair undergoes annihilation in a very short time. Notice that a logarithmic scale is used in this figure in order to highlight the vortex positions, which would otherwise be invisible in an ordinary plot. The results presented in Fig. 15 are for $a_s = 93\ a_0$ and initial intervortex distance $d = 4a$, where $a = 3.44\ \mu$m is the lattice parameter of the SSP for this a_s value. We also considered a different, more symmetric initial configuration of the two vortices, i.e., the case where the two vortices are positioned along the y axis of Fig. 15 and separated directly by a droplet. In spite of the symmetric initial configuration of the two vortices, which might suggest the possibility of a metastable state where the two vortices remain pinned there, the combined velocity field starts displacing both vortices to the right (it would be the left for interchanged vortex signs), and then they almost immediately annihilate each other. We have found that similar dynamics of the vortex dipole occurs for other values of d and a_s corresponding to a SSP. Therefore, the disclosed annihilation process of two counterrotating vortices appears to be generic for the SSP of dipolar bosons.

By following the snapshots in Fig. 15, one can see that the recombination process proceeds by a set of jumps from one interstitial site to a neighboring one and that in the jump process, each vortex becomes elongated by extending over the two neighboring sites as well as over the in-between saddle point. Since the snapshots represent the projected density on the x-y plane, one can ask if the elongation of the vortex during the jump is due to propagation of kinks along the vortex axis, as discussed in the previous section, or if the vortex rigidly translates from one site to another one. We find that this second case indeed occurs since we have verified that the density in single x-y planes has exactly the same dynamics as the projected one.
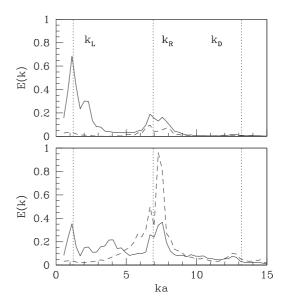
The energy released immediately after the annihilation goes into excitations of the droplet array, which appears to be deformed and oscillating after the recombination event. Such change in the character of the excitation energy can be characterized by computing the spectral density of the kinetic energy of the superfluid velocity field, decomposing it into compressible and incompressible parts [54,55] by utilizing the Helmholtz decomposition theorem. We show in Fig. 16 these two contributions as a function of the wave vector in the x-y plane k, where we have taken a time average over the first 40 ms of the dynamics, which corresponds to times before vortex annihilation, and over 20 ms after vortex annihilation. The vertical lines show three relevant wave vectors: $k_L = 2\pi/L$, where $L = \sqrt{L_x L_y}$ is the average size of the simulation cell; $k_R = 2\pi/a$, which is the wave vector corresponding to the periodic arrangement of droplets (a being the droplet-droplet nearest-neighbor distance in the SSP); and $k_D = 2\pi/D$, where D is the average droplet diameter. One can see that when the vortex dipole is present (first time interval), the main contribution to the spectral density is in the incompressible component at rather small k. In particular, the peak at k_L is related to the cell size through the periodic boundary conditions. After the vortex dipole annihilation, the main contribution is transferred into the compressible component at k values, $\sim k_R$, which corresponds to the k value associated with solid order. A similar roton burst has been observed in the annihilation of vortex dipoles in superfluid ^{4}He nanodroplets [56].

VI. SUMMARY

It is now well established that dipolar bosons, in addition to a superfluid state, can be in a supersolid state in which the local density of the condensate is modulated in the plane

perpendicular to the polarization direction. This phase appears when the strength of the dipolar interaction is strong enough compared to the contact interaction. The supersolid state consists of a regular array of droplets and a low-density superfluid background which occupies the space between them.

In order to determine the intrinsic properties of vortices in the SSP, we have studied the system without trapping potential in the x-y plane, but with suitable boundary conditions in the computation cell, and a harmonic trap is present only in the z direction, i.e., the polarization direction. We have determined the equilibrium lattice parameter and the superfluid fraction of this extended system of dipolar bosons for different values of the s-wave scattering length. We have found that a singly quantized, linear vortex along the polarization direction is a stable excitation of the system in a stationary state. A fundamental property of a vortex in the supersolid state is that it has equilibrium positions in the crystalline structure of the bosons; in our case, at the interstitial sites of the triangular droplets lattice.

We have characterized the density profile of the vortex, its velocity field, and the kinetic energy as a function of the distance from the vortex core. The velocity field strongly differs from the simple circular flow in a superfluid. In addition, most of the contribution to the quantum of circulation in the SSP is due to the low-density background, with the droplets giving only a small contribution to it.

As the ratio of the dipolar to the contact interaction increases, the vortex core expands and the core energy decreases. We have computed the energy barrier that a vortex has to surmount to move from an equilibrium site to a neighboring one. The existence of this energy barrier—and the density modulation due to the presence of droplets—represents a major difference from a uniform superfluid in which a vortex is free to move when it is far from the boundaries. The dynamics of vortices in a dipolar superfluid has been predicted [57] to differs from that in a standard BEC. Even stronger modifications of the vortex dynamics are expected in a supersolid. In a SSP, such dynamics should be characterized by oscillations around the equilibrium position and by jumps from one site to another.

We have explored one particular aspect of the vortex dynamics, namely, the behavior of a vortex dipole made of two counter-rotating parallel vortices. In a uniform superfluid, the vortex dipole is a stable entity which rigidly translates with constant velocity. We have found that in the SSP, the vortex dipole is an unstable excitation; the two vortices of opposite chirality do not translate, but they approach each other by a series of jumps until they annihilate and the excitation energy goes into bulk excitation of the supersolid. We believe that this is just an example of different features of the vortex dynamics in a supersolid. For instance, Kelvin waves, i.e., the basic excitations of a vortex, should be strongly modified in the SSP with respect to the SFP and a different kind of excitation might arise, at least when the droplets are elongated enough, consisting of kinks of the vortex core transferring the core of the vortex from one equilibrium site to another.

Finally, it should also be noticed that the periodic boundary conditions in the plane perpendicular to the polarization direction impose a constraint on the spatial order of the droplets, so that they cannot rotate even when a vortex is present. However, we believe that this is not an artifact of boundary conditions. In fact, we have verified that a single vortex is also a (meta)stable excitation when the system is confined in the x-y plane by a cylindrically symmetric trap. We find that the droplets also do not rotate during the typical lengths of our simulation, of the order of several tens of milliseconds. This gives evidence for the existence of an excitation with the vortex phase singularity at the center of the bucket with a stationary supersolid structure. This behavior is at variance with the state of dipolar bosons in a rotating trap which induces single or multiple vortices [34,38,39] with the whole supersolid structure set in rotation. It will be interesting to study the behavior of a vortex dipole for other systems in a SSP, especially if the spatial order is different from that of dipolar bosons.

[1] R. J. Donnelly, *Quantized Vortices in Helium II* (Cambridge University Press, Cambridge, 1991).

[2] C. F. Barenghi, R. J. Donnelly, and W. F. Vinen, *Quantized Vortex Dynamics and Superfluid Turbulence* (Springer Science and Business Media, Berlin, 2001).

[3] A. L. Fetter, Rev. Mod. Phys. **81**, 647 (2009).

[4] L. Pitaevskii and S. Stringari, *Bose-Einstein Condensation and Superfluidity*, International Series of Monographs on Physics Vol. 164 (Oxford University Press, Oxford, 2016).

[5] S. Balibar, Nature (London) **464**, 176 (2010).

[6] A. F. Andreev and I. M. Lifshitz, Sov. Phys. JETP **29**, 1107 (1969).

[7] G. V. Chester, in *Lectures in Theoretical Physics*, edited by K. T. Mahanthappa and W. E. Britten (Gordon & Breach, New York, 1969); G. V. Chester, Phys. Rev. A **2**, 256 (1970).

[8] A. J. Leggett, Phys. Rev. Lett. **25**, 1543 (1970).

[9] M. H. W. Chan, R. B. Hallock, and L. Reatto, J. Low Temp. Phys. **172**, 317 (2013); **173**, 354(E) (2013).

[10] M. Boninsegni and N. V. Prokof'ev, Rev. Mod. Phys. **84**, 759 (2012).

[11] H. Lamb, *Hydrodynamics* (Dover, New York, 1945).

[12] L. Santos, G. V. Shlyapnikov, and M. Lewenstein, Phys. Rev. Lett. **90**, 250403 (2003).

[13] D. H. J. O'Dell, S. Giovanazzi, and G. Kurizki, Phys. Rev. Lett. **90**, 110402 (2003).

[14] M. Wenzel, F. Bottcher, T. Langen, I. Ferrier-Barbut, and T. Pfau, Phys. Rev. A **96**, 053630 (2017).

[15] D. Baillie and P. B. Blakie, Phys. Rev. Lett. **121**, 195301 (2018).

[16] L. Chomaz, R. M. W. van Bijnen, D. Petter, G. Faraoni, S. Baier, J. H. Becher, M. J. Mark, F. Wächtler, L. Santos, and F. Ferlaino, Nat. Phys. **14**, 442 (2018).

[17] Y. Kora and M. Boninsegni, J. Low Temp. Phys. **197**, 337 (2019).

[18] S. M. Roccuzzo and F. Ancilotto, Phys. Rev. A **99**, 041601(R) (2019).

[19] H. Kadau, M. Schmitt, M. Wenzel, C. Wink, T. Maier, I. Ferrier-Barbut, and T. Pfau, Nature (London) **530**, 194 (2016).

[20] I. Ferrier-Barbut, H. Kadau, M. Schmitt, M. Wenzel, and T. Pfau, Phys. Rev. Lett. **116**, 215301 (2016).

[21] M. Schmitt, M. Wenzel, F. Böttcher, I. Ferrier-Barbut, and T. Pfau, Nature (London) **539**, 259 (2016).

[22] F. Wächtler and L. Santos, Phys. Rev. A **93**, 061603(R) (2016).

[23] D. Baillie, R. M. Wilson, R. N. Bisset, and P. B. Blakie, Phys. Rev. A **94**, 021602(R) (2016).

[24] L. Chomaz, S. Baier, D. Petter, M. J. Mark, F. Wachtler, L. Santos, and F. Ferlaino, Phys. Rev. X **6**, 041039 (2016).

[25] A. R. P. Lima and A. Pelster, Phys. Rev. A **84**, 041604(R) (2011).

[26] R. Bombin, J. Boronat, and F. Mazzanti, Phys. Rev. Lett. **119**, 250402 (2017).

[27] F. Cinti and M. Boninsegni, Phys. Rev. A **96**, 013627 (2017).

[28] Y.-C. Zhang, F. Maucher, and T. Pohl, Phys. Rev. Lett. **123**, 015301 (2019).

[29] L. Chomaz, D. Petter, P. Ilzhöfer, G. Natale, A. Trautmann, C. Politi, G. Durastante, R. M. W. van Bijnen, A. Patscheider, M. Sohmen, M. J. Mark, and F. Ferlaino, Phys. Rev. X **9**, 021012 (2019).

[30] F. Böttcher, J.-N. Schmidt, M. Wenzel, J. Hertkorn, M. Guo, T. Langen, and Tilman Pfau, Phys. Rev. X **9**, 011051 (2019).

[31] L. Tanzi, E. Lucioni, F. Fama, J. Catani, A. Fioretti, C. Gabbanini, R. N. Bisset, L. Santos, and G. Modugno, Phys. Rev. Lett. **122**, 130405 (2019).

[32] L. Tanzi, S. M. Roccuzzo, E. Lucioni, F. Fama, A. Fioretti, C. Gabbanini, G. Modugno, A. Recati, and S. Stringari, Nature (London) **574**, 382 (2019).

[33] L. Tanzi, J. G. Maloberti, G. Biagioni, A. Fioretti, G. Gabbanini, and G. Modugno, Science **371**, 1162 (2021).

[34] S. M. Roccuzzo, A. Gallemi, A. Recati, and S. Stringari, Phys. Rev. Lett. **124**, 045702 (2020).

[35] P. Ilzhöfer, M. Sohmen, G. Durastante, C. Politi, A. Trautmann, G. Morpurgo, T. Giamarchi, L. Chomaz, M. J. Mark, and F. Ferlaino, arXiv:1912.10892

[36] Y. Pomeau and S. Rica, Phys. Rev. Lett. **72**, 2426 (1994); N. Sepulveda, C. Josserand, and S. Rica, Eur. Phys. J. B **78**, 439 (2010).

[37] M. Guo, F. Böttcher, J. Hertkorn, J.-N. Schmidt, M. Wenzel, H. P. Büchler, T. Langen, and T. Pfau, Nature (London) **574**, 386 (2019).

[38] A. Gallemi, S. M. Roccuzzo, S. Stringari, and A. Recati, Phys. Rev. A **102**, 023322 (2020).

[39] F. Ancilotto, M. Barranco, M. Pi, and L. Reatto, arXiv:2002.05934.

[40] C. A. Jones and P. H. Roberts, J. Phys. A **15**, 2599 (1982); A. Griffin, V. Shukla, M.-E. Brachet, and S. Nazarenko, Phys. Rev. A **101**, 053601 (2020).

[41] F. Ancilotto, M. Barranco, F. Coppens, J. Eloranta, N. Halberstadt, A. Hernando, D. Mateo, and M. Pi, Intl. Rev. Phys. Chem. **36**, 621 (2017).

[42] T. Lahaye, C. Menotti, L. Santos, M. Lewenstein, and T. Pfau, Rep. Progr. Phys. **72**, 126401 (2009).

[43] M. Pi, R. Mayol, A. Hernando, M. Barranco, and F. Ancilotto, J. Chem. Phys. **126**, 244502 (2007).

[44] M. Sadd, G. V. Chester, and L. Reatto, Phys. Rev. Lett. **79**, 2490 (1997).

[45] F. Ancilotto, M. Barranco, and M. Pi, Phys. Rev. B **97**, 184515 (2018).

[46] S. Yi and H. Pu, Phys. Rev. A **73**, 061602(R) (2006).

[47] I. Amelio, D. E. Galli, and L. Reatto, Phys. Rev. Lett. **121**, 015302 (2018).

[48] A. Cidrim, F. E. A. dos Santos, E. A. L. Henn and T. Macri, Phys. Rev. A **98**, 023618 (2018).

[49] D. E. Galli, L. Reatto, and M. Rossi, Phys. Rev. B **89**, 224516 (2014).

[50] A. L. Fetter, Phys. Rev. A **69**, 043617 (2004).

[51] J. Beamish and S. Balibar, Rev. Mod. Phys. **92**, 045002 (2020).

[52] T. W. Neely, E. C. Samson, A. S. Bradley, M. J. Davis, and B. P. Anderson, Phys. Rev. Lett. **104**, 160401 (2010); D. V. Freilich, D. M. Bianchi, A. M. Kaufman, T. K. Langin, and D. S. Hall, Science **329**, 1182 (2010).

[53] F. Ancilotto, M. Barranco, J. Eloranta, and M. Pi, Phys. Rev. B **96**, 064503 (2017).

[54] C. Nore, M. Abid, and M. E. Brachet, Phys. Fluids **9**, 2644 (1997).

[55] M. Tsubota, K. Fujimoto, and S. Y. Tsubota, J. Low. Temp. Phys. **188**, 119 (2017).

[56] J. M. Escartin, F. Ancilotto, M. Barranco, and M. Pi, Phys. Rev. B **99**, 140505(R) (2019).

[57] B. C. Mulkerin, R. M. W. van Bijnen, D. H. J. O'Dell, A. M. Martin, and N. G. Parker, Phys. Rev. Lett. **111**, 170402 (2013).